Eur. Phys. J. B **78**, 439–447 (2010)
DOI: 10.1140/epjb/e2010-10176-y

THE EUROPEAN PHYSICAL JOURNAL B

Regular Article

Superfluid density in a two-dimensional model of supersolid

N. Sepúlveda[1,2], C. Josserand[2,a], and S. Rica[3,4]

[1] Laboratoire de Physique Statistique, École Normale Supérieure, UPMC Paris 06, Université Paris Diderot, CNRS, 24 rue Lhomond, 75005 Paris, France
[2] Institut Jean Le Rond D'Alembert, UMR 7190 CNRS-UPMC, 4 place Jussieu, 75005 Paris, France
[3] Facultad de Ingeniería y Ciencias, Universidad Adolfo Ibáñez, Avda. Diagonal las Torres 2640, Peñalolén, Santiago, Chile
[4] INLN, CNRS-UNSA, 1361 route des Lucioles, 06560 Valbonne, France

Received 28 February 2010 / Received in final form 27 October 2010
Published online 6 December 2010 –

Abstract. We study in 2-dimensions the superfluid density of periodically modulated states in the framework of the mean-field Gross-Pitaevskiĭ model of a quantum solid. We obtain a full agreement for the superfluid fraction between a semi-theoretical approach and direct numerical simulations. As in 1-dimension, the superfluid density decreases exponentially with the amplitude of the particle interaction. We discuss the case when defects are present in this modulated structure. In the case of isolated defects (e.g. dislocations) the superfluid density only shows small changes. Finally, we report an increase of the superfluid fraction up to 50% in the case of extended macroscopical defects. We show also that this excess of superfluid fraction depends on the length of the complex network of grain boundaries in the system.

1 Introduction

Superfluidity is a crucial property at low temperature of many quantum liquids or gases such as liquid Helium or Bose-Einstein condensates. On the contrary, the question of superfluidity in crystalline structures remains more complicated since the varying density inhibits the quantum phase coherence. This phenomenon, called "supersolidity", has been matter of large speculation for the last forty years, since seminal works of Andreev-Lifshitz, Reatto, Chester and Leggett [1–4]. Today, after the breakthrough experiments by Kim and Chan [5–7] supersolidity appears as a new striking feature of solid Helium below 100 mK. As originally established [4], supersolidity is manifested through the loss of a fraction of the moment of inertia of a torsional oscillator filled by solid Helium. This non classical rotational inertia (NCRI), which is an important property of superfluid systems, has nowadays been confirmed by more than six different experimental groups [8–13], using different geometries and conditions. However, it seems that the whole story – from theoretical and experimental points of view – is far from over. Essentially, a coherent theoretical framework that would account the experimental findings is still lacking. In fact many open questions need clarifications at least at a fundamental level.

In particular: what are the features of the wave function to display or not superfluidity? It is well known that Chester-Reatto wavefunction displays off diagonal long range order (ODLRO) [2,3], thus NCRI. However, it has been suggested, using quantum Monte-Carlo numerical models, that a perfect crystal of helium atoms cannot exhibit a supersolid behavior, since local exchange does not produce a finite NCRI in the thermodynamic limit [14,15]. In fact, there is no insight yet of any microscopic mechanism explaining supersolidity and the Bose-Einstein condensation of vacancies, early proposed by Andreev and Lifshitz [1], is still questioned [16]. The unknown complex structure of the solid helium ground state wave function makes this challenge difficult and therefore a general theory of supersolidity of solid helium – if it is supersolidity that explains the experimental observations – is still far from reachable. In this sense, a substantially less ambitious subject is the study of supersolidity in more simple systems than solid helium, such as cold atoms. There, one replaces a crystal structure by a density modulated system. Density modulated Bose-Einstein condensates are currently formed by the imposition of an external potential, creating the so-called optical lattices [17,18]. In these cases, by varying the properties of the optical lattice, the condensate is shown to exhibit a Mott insulator/superfluid phase transition [17–20]. More recently, it has also been suggested recently that supersolidity might be present for Rydberg atoms in dipole-blockade regime [21,22]. In reference [21] the authors take an artificial interaction potential which allow a ground-state computation, which happens to display the properties of supersolidity proving that, under some conditions, a quantum system of interacting particles exhibits a crystalline structure and the superfluidity property. The present article concerns thus the study of the superfluid density in the framework of cold atoms where a mean field theory can be applied.

[a] e-mail: josseran@lmm.jussieu.fr

A model for density modulated quantum system can be obtained in the general framework of the Gross-Pitaevskiĭ (GP) equation [23,24], using a non-local [25,26] or an external [17,18] potential. This mean-field GP equation can be deduced for Bose-Einstein condensates using the dilute gas approximation which assumes that the N body wave function, $\Psi_N(\boldsymbol{r}_1, \boldsymbol{r}_2, \dots \boldsymbol{r}_N)$, is factorized in terms of a single "condensate wave function" $\psi(\boldsymbol{r})$, such that

$$\Psi_N(\boldsymbol{r}_1, \boldsymbol{r}_2, \dots \boldsymbol{r}_N) = \psi(\boldsymbol{r}_1) \times \psi(\boldsymbol{r}_2) \times \cdots \times \psi(\boldsymbol{r}_N).$$

This approximation cannot apply formally to Helium atoms although such models have commonly been used to describes the dynamics of Helium at low temperature. Superfluidity is then an inherent property of the GP model as it can be proved using the Leggett calculation of the NCRIF lower bound [27]. Thus, the GP equation describes the evolution of a wave-function that exhibits, even without an external potential, both crystallisation of the system (thus a solid) and a coherent quantum phase (showing superfluidity): this is a supersolid showing in particular the NCRI property [26]. As discussed above, the striking property of this model is not to exhibit the superfluidity, but rather the elastic behavior such as a solid [28]. In the same spirit, Anderson [29] has recently considered a Gross-Pitaevskii theory for a weakly interacting Bose-Einstein condensate of vacancies displaying the superfluid property responsible of the non classical rotational inertia. Despite the fact that vacancies attract themselves [16], so that the superfluid is unstable in the long wave regime, the basic crystal structure of the solid is not considered in this model so that the coupling between the condensate and the crystal displacements are not taken into account.

By developing the long wave dynamics, we have obtained from the GP equation a macroscopic model of a supersolid, coupling the elastic properties of the solid with the quantum phase [26,28]. We want to emphasize here that the pertinence of this macroscopic approach goes beyond the details of the GP model and has been proposed elsewhere with different methods [30]. In [31] we have studied this Gross-Pitaevskii model of supersolid in 1-dimension, using both direct numerical simulations and analytical estimates for the ground state solution. We have compared the ground state characteristics such as the peak size, obtained via variational arguments, with direct numerical calculations showing an impressively good agreement. Considering periodic systems, we have computed the NCRIF using both the Leggett quotient [4], and direct numerical simulations, with full quantitative agreement. Thanks to such comparisons, we have shown that for the GP equation in 1-dimension the NRCIF decreases exponentially when increasing the dimensionless interaction parameter (Λ defined later in Eq. (7)). More precisely, the superfluid fraction follows $\log f_{ss} \sim -\sqrt{\Lambda}$ for large Λ because of the exponentially small dependence of the profile of the ground state density with Λ.

In this paper, we present a detailed study of this model in 2-dimensions. As for the 1-dimension case, the aim of the study is first to compare semi-analytical estimates of the superfluid fraction using homogenization techniques with the direct numerical calculation of the superfluid fraction. Here we find that the superfluid fraction decreases again with Λ, $\log f_{ss} \sim -\sqrt{\Lambda}$, at least for moderate values of Λ, as in 1-dimension. For higher values of Λ, it is harder to draw a strong conclusions from our results. However, beside these needed technical but interesting aspects of comparing the semi-analytical macroscopic approach with the direct numerical calculations, 2-dimensions is crucial because it is the lowest relevant spatial dimension to investigate and to disentangle the contribution of the crystal defects to the superfluid fraction. Indeed, although the NCRI feature has always been experimentally noticed, the large variability of the amount of the NCRI fraction (NCRIF) as the geometries or the solid samples change, gives rise to a large scientific debate. The nature of the supersolidity is questioned as well as its dependence on the specific properties of the solid crystal structure (presence of defects or vacancies in particular) [1,3,13,26,32–34]. For instance, the macroscopic superflow can be dominated by multiple distinct paths that may avoid the absolute minimum of the wave function. In the last section, we show how the presence of defects enhance the supersolid fraction in the model, with qualitative agreement with the experimental observations.

2 The Gross-Pitaevskii equation with a nonlocal interaction potential

The original GP equation [24] for the complex wave function $\psi(\boldsymbol{x}, t)$ in 2D is:

$$i\hbar\frac{\partial\psi}{\partial t} = -\frac{\hbar^2}{2m}\nabla^2\psi + \psi(\boldsymbol{x}, t)\int U(|\boldsymbol{x}-\boldsymbol{y}|)|\psi(\boldsymbol{y})|^2 d\boldsymbol{y}. \quad (1)$$

Equation (1) describes, by a mean-field approximation, the evolution of the wave-function $\psi(\boldsymbol{x}, t)$ where $U(r)$ is the two body potential between the atoms.

The evolution (1) is Hamiltonian,

$$i\hbar\partial_t\psi = \frac{\delta H}{\delta\psi^*},$$

with the energy or Hamiltonian

$$H = \frac{\hbar^2}{2m}\int |\boldsymbol{\nabla}\psi|^2 d\boldsymbol{x} + \frac{1}{2}\int U(|\boldsymbol{x}-\boldsymbol{y}|)|\psi(\boldsymbol{y})|^2|\psi(\boldsymbol{x})|^2 d\boldsymbol{y}d\boldsymbol{x}. \quad (2)$$

This energy H, the number of particles N,

$$N = \int |\psi(\boldsymbol{x})|^2 d\boldsymbol{x}, \quad (3)$$

and the linear momentum $\boldsymbol{P}$,

$$\boldsymbol{P} = -\frac{i\hbar}{2}\int (\psi^*\boldsymbol{\nabla}\psi - \psi\boldsymbol{\nabla}\psi^*) d\boldsymbol{x}, \quad (4)$$

are conserved by the dynamical evolution of (1). According to the energy dependence on the phase of the wave

function, one notices that the ground state solution is always real since any non uniform phase increases its energy.

Consider now a homogeneous solution $\psi_0 = \sqrt{n_0}e^{-i\frac{E_0}{\hbar}t}$, with n_0 the mean density and $E_0 = 2\pi n_0 \int_0^\infty U(r)rdr$. Then the perturbations around this homogeneous solution give dispersive waves with a dispersion relation following the Bogoliubov spectrum relation [35]:

$$\hbar\omega_k = \sqrt{\left(\hbar^2k^2/2m\right)^2 + \left(\hbar^2k^2/m\right)n_0\hat{U}_k}, \tag{5}$$

where $\hat{U}_k$ is the Fourier transform that has to be bounded for all k:

$$\begin{aligned}\hat{U}_k &= \int_0^\infty \int_0^{2\pi} U(r)e^{ikr\cos\theta}\, r\, dr\, d\theta \\ &= 2\pi \int_0^\infty U(r)J_0(k\,r)\, r\, dr. \end{aligned} \tag{6}$$

Remarkably, the spectrum (5) depends only on a single dimensionless parameter [25]:

$$\Lambda = n_0 \frac{ma^2}{\hbar^2}\hat{U}_{\boldsymbol{k}=0} \tag{7}$$

denoting a the characteristic length scale of the potential. To allow stability of the long wave modes, the potential $U(r)$ has also to satisfy:

$$0 < 2\pi \int_0^\infty U(r)rdr = \hat{U}_{\boldsymbol{k}=0} < \infty.$$

Moreover, we shall require that $\hat{U}_k$ becomes negative at some k_c to allow for the roton crystallization mechanism [36–38]. For instance in the numerics later on, we choose the soft core interaction, with no loss of generalities (although in the case of Rydberg atoms [21,22] the interaction possesses a long range tail $1/r^3$ in 2-dimensions, the roton spectrum (5) does not change substantially):

$$U(|\boldsymbol{x}-\boldsymbol{y}|) = U_0\theta(a-|\boldsymbol{x}-\boldsymbol{y}|), \tag{8}$$

with $\theta(\cdot)$ the Heaviside function. In 2D, the Fourier transform of this special interaction potential writes:

$$\hat{U}_k = 2\pi U_0 a \frac{J_1(ka)}{k},$$

where J_1 is the Bessel function of the first kind. $\hat{U}_{\boldsymbol{k}=0} = \pi a^2 U_0$, so that $\Lambda = n_0\frac{\pi m a^4}{\hbar^2}U_0$ in this special case.

We emphasize that the special choice of the potential (8) is purely of practical interest because it is easy to implement in numerical schemes. Other functions whose Fourier transform would be negative for a wave number domain (strictly bigger than zero), would show similar properties. In particular, it is possible to find the potential such that the Bogoliubov dispersion relation matches the Landau spectrum with the right values of the speed of sound c, and the three roton parameters [25].

With $\boldsymbol{x}' = \boldsymbol{x}/a$, $t' = \frac{\hbar}{ma^2}t$, and $\psi' = \psi/\sqrt{n_0}$, the dimensionless GP equation for the Heaviside interaction (we drop the primes hereafter) reads:

$$i\frac{\partial\psi}{\partial t} = -\frac{1}{2}\nabla^2\psi + \Lambda\,\psi(\boldsymbol{x},t)\int \Theta(|\boldsymbol{x}-\boldsymbol{y}|)|\psi(\boldsymbol{y})|^2 d\boldsymbol{y}, \tag{9}$$

where $\Theta(|\boldsymbol{x}-\boldsymbol{y}|) = \frac{1}{\pi}\theta(1-|\boldsymbol{x}-\boldsymbol{y}|)$.

In the following, we consider a square domain: $\Omega = [0,L]\times[0,L]$ with periodic boundary conditions $\psi(x,y,t) = \psi(x+L,y,t)$ and $\psi(x,y,t) = \psi(x,y+L,t)$. Note that here L is dimensionless.

We then define the energy and number of particles densities of the system:

$$\begin{aligned}\mathcal{E} = \frac{1}{2\Omega}\int_\Omega |\nabla\psi|^2\, d\boldsymbol{x} + \frac{\Lambda}{2\Omega}\int_\Omega \Theta(|\boldsymbol{x}-\boldsymbol{y}|)|\psi(\boldsymbol{y})|^2 \\ \times |\psi(\boldsymbol{x})|^2 d\boldsymbol{y}d\boldsymbol{x}, \end{aligned} \tag{10}$$

$$\mathcal{N} = \frac{1}{\Omega}\int_\Omega |\psi(\boldsymbol{x},t)|^2 d\boldsymbol{x} = 1, \tag{11}$$

which are the relevant control parameters of the system.

3 The ground state and macroscopic equations

For large enough values of Λ, equation (9) displays modulated structure solutions. We recall in this section the results deduced for the dynamics near this modulate ground state [25,26,28].

3.1 Ground state

The ground state can be determined by minimizing the energy functional (10) together with the constraint (11): in general this ground state exists and provides a pure real and positive wave function. For low values of Λ the ground state is homogeneous in space: that is a liquid without positional order. As Λ increases there is a critical value where the liquid phase (the homogenous solution) is no longer the lowest energy solution. There, the competition between the non-local interaction and the kinetic term in equation (10) allows for the formation of density gradients such that the energy is then lower than the one of the homogenous solution. In reference [25] a weakly nonlinear analysis exhibited the formation of a crystalline structure for large enough Λ in two and three spatial dimensions. In 2-dimensions for the potential (8) the crystal appears for $\Lambda \gtrsim 41.6$. For larger Λ, the ground state becomes a periodic structure of well defined tiny peaks (see Fig. 1). In the large Λ limit, this ground state can even be described as a solution of the 2-dimensional packing problem [39].

3.2 Macroscopic equations

To obtain the dynamical properties of this crystal, we need to extract the long and slow variation of the solution from the periodic structure. In references [26,28], we

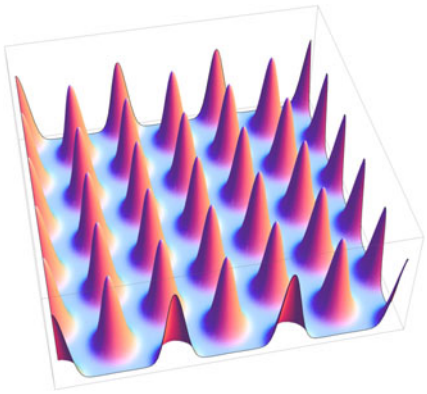

Fig. 1. (Color online) Ground state for a 2D system with periodic boundary conditions. This ground state correspond to $\Lambda = 82.36$ an average density $\frac{1}{L^2}\int_0^L \int_0^L |\psi(x,y)|^2\, dx\, dy = 1$. The total size of the system is $L = 64$ units and the range of interaction is $a = 16$. The system displays 30 peaks.

have described these low energy excitations around the ground state: expanding the solution as a slowly and large-scale varying crystal structure, and using homogenization techniques [40], we have obtained a set of macroscopic equations for the mean density $\rho(\boldsymbol{x},t)$, the coherent phase $\Phi(\boldsymbol{x},t)$ and the elastic deformation $\boldsymbol{u}(\boldsymbol{x},t)$ of the crystal:

$$\frac{\partial \rho}{\partial t} + \frac{\partial}{\partial x_i}\left(\varrho^{ss}_{ik}\frac{\hbar}{m}\partial_k\Phi + (\rho\delta_{ik} - \varrho^{ss}_{ik})\dot{u}_k\right) = 0 \tag{12}$$

$$m\frac{\partial}{\partial t}\left[(\rho\delta_{ik} - \varrho^{ss}_{ik})\left(\dot{u_k} - \frac{\hbar}{m}\partial_k\Phi\right)\right] + \hbar\frac{\partial}{\partial x_k}\left[(\rho\delta_{il} - \varrho^{ss}_{il})\left(\dot{u}_l - \frac{\hbar}{m}\partial_l\Phi\right)\partial_k\Phi\right] = \frac{\partial}{\partial x_k}\left(\lambda_{iklm}u_{lm}\right) \tag{13}$$

$$\hbar\frac{\partial\Phi}{\partial t} + \frac{\hbar^2}{2m}(\boldsymbol{\nabla}\Phi)^2 + \mathcal{E}'(\rho) = 0, \tag{14}$$

where $u_{ik} = \frac{1}{2}(\partial_i u_k + \partial_k u_i)$ is the usual strain tensor in the theory of elasticity, $\dot{u}_i = \partial_t u_i + \frac{\hbar}{m}\partial_k\Phi\partial_k u_i$ is the covariant time derivative of the elastic deformation u_i and ϱ^{ss}_{il} is the superfluid tensor. The set of equations (12–14) is in fact a simplified (the linearized) version of the general macroscopic model where some nonlinear terms have been dropped for the sake of clarity. The parameters in these macroscopical equations, such as the elastic modulus λ_{iklm}, the chemical potential $\mathcal{E}'(\rho)$ and the superfluid density ϱ^{ss}_{ik} do depend on the local density, ρ, and can be computed ab-initio from knowledge of the underlying crystal structure [28]. Practically, these parameters are obtained by solving differential equations at the level of a unit cell of the periodic structure, characterized by the wave function of the ground state $\psi_0(\boldsymbol{x})$. In this article, we focus on the behavior of the superfluid density ϱ^{ss}_{ik} for which we will show its resolution in details below. Equation (12) is the mass conservation equation for the total density ρ, with the current $j_i = \varrho^{ss}_{ik}v^s_k + (\rho\delta_{ik} - \varrho^{ss}_{ik})\dot{u}_k$ and where we have defined the "superfluid velocity" $\boldsymbol{v}^s = \frac{\hbar}{m}\boldsymbol{\nabla}\Phi$. Equation (13) is the usual equation for the elastic response of the system. If the phase $\Phi(\boldsymbol{x},t)$ can be neglected, one recovers the usual equation for the elastic deformation of macroscopical bodies. Finally, equation (14) is a Bernoulli like equation for the quantum phase, that gives the usual Landau equation for the superfluid velocity $\partial_t\boldsymbol{v}^s = -\boldsymbol{\nabla}\left(\frac{\boldsymbol{v}^{s\,2}}{2} + \mathcal{E}'(\rho)\right)$. Thus, this macroscopic set of equations shows that the GP equation (9) can model a system that shows both superfluidity (if we find a non-zero ϱ^{ss}_{ik}) and the usual elasticity of solid bodies.

3.3 Superfluid density

In reference [28] we have obtained, using a homogenization technique [40], an expression for the superfluid density matrix ϱ^{ss}_{ik} deduced directly from the ground state density profile of the crystal $\rho_0(\boldsymbol{x}) = |\psi_0(\boldsymbol{x})|^2$. The superfluid fraction tensor is:

$$f^{ss}_{ik} = \frac{\varrho^{ss}_{ik}}{\rho} = \delta_{ik} - \frac{\int_V \rho_0(\boldsymbol{x})\ (\boldsymbol{\nabla}K_i\cdot\boldsymbol{\nabla}K_k)\ d\boldsymbol{x}}{\int_V \rho_0(\boldsymbol{x})\, d\boldsymbol{x}}, \tag{15}$$

where the auxiliary functions K_k (two in two space dimensions) are defined only in the unitary lattice cell V and satisfy:

$$\partial_k\rho_0 + \boldsymbol{\nabla}\cdot(\rho_0(\boldsymbol{x})\boldsymbol{\nabla}K_k) = 0 \quad \text{in}\, V \tag{16}$$

with periodic boundary condition at the frontier of the cell.

If the crystal modulation is absent ($\rho_0(\boldsymbol{x}) = \text{const.}$), then $K_x = K_y = 0$ (up to constants) so that the superfluid fraction tensor $f^{ss}_{ik} \to \delta_{ik}$. In general, there is no formal solution to the problem (15, 16) for an arbitrary $\rho_0(\boldsymbol{x})$ in any spatial dimension (the only exception is the 1-dimension case, see [31]). However, because of the elliptic character of equations (16), since $\rho_0(\boldsymbol{x}) > 0$, the symmetric matrix f^{ss}_{ik} can easily be computed numerically.

On the other hand, the superfluid fraction can also be defined directly through the momentum carried by the superfluid part. The total momentum, from (4), is

$$P_i = \hbar\int\rho_0(\boldsymbol{x})\boldsymbol{\nabla}_i\phi\, d\boldsymbol{x} = mv_k\int\rho_0(\boldsymbol{x})(\delta_{ik} + \partial_i K_k)\, d\boldsymbol{x} \tag{17}$$

and one gets the same definition of the superfluid fraction since: $P_i = m\int\rho_0(\boldsymbol{x})\, d\boldsymbol{x} f^{ss}_{ik}\, v_k$.

4 Numerical computations of the ground state and the superfluid density matrix

4.1 Ground state of the system

The numerical results are obtained by minimizing the energy equation (10) under the number of particles condition equation (11). For this purpose, we use the Ginzburg-Landau (GL) version of the dynamics which can be interpreted as the integration of the GP equation for imaginary time $t = -\imath\tau$:

$$\frac{\partial\psi}{\partial\tau} = \mu\psi + \frac{1}{2}\nabla^2\psi - \Lambda\psi(\boldsymbol{x},t)\int_\Omega \Theta(|\boldsymbol{x}-\boldsymbol{y}|)|\psi(\boldsymbol{y})|^2 d\boldsymbol{y}, \tag{18}$$

where μ is the Lagrangian multiplier introduced to satisfy the number of particles condition (11). Note that the total momentum of the ground state is zero. We use a pseudo-spectral numerical scheme, where the linear dynamics is computed in the Fourier space while the non-linear part is performed in real space. The Lagrange multiplier is found by a Newton method to reach the correct total number of particles. The Fourier transforms are computed using the FFTW library[1].

Figure 1 shows the ground state computed for $\Lambda = 82.36$ in a 64×64 periodic box. This ground state forms an hexagonal pattern of 30 peaks.

4.2 Numerical computation of superfluid density following the solution of K_x and K_y

In this section, we present the numerical calculation of the superfluid fraction through the formalism of the homogenization described above. We need to calculate $K_i(\boldsymbol{x})$ from (16) with periodic boundary conditions on the opposite faces of the hexagonal unit cell V. To do this we use a finite element method: we first extract from the numerics the ground state $\rho_0(\boldsymbol{x})$ in the unit cell V. Next, we build a triangular mesh inside the unit cell and we have used $n_v = 100$ vertices for the triangular mesh on which we have extrapolated the above ground state density ρ_0 obtained by minimizing the GP energy. Next, we solve equation (16) in a variational form by multiplying (16) with an arbitrary function $v(\boldsymbol{x})$ periodic in V. Integrating over V, we obtain the two equations (for $i = 1, 2$):

$$\int_V \left[\rho_0(\boldsymbol{x})\nabla K_i(\boldsymbol{x}) \cdot \nabla v(\boldsymbol{x}) - \partial_i \rho_0(\boldsymbol{x}) v(\boldsymbol{x})\right] d\boldsymbol{x} = 0, \quad (19)$$

valid for every periodic function $v(\boldsymbol{x})$ defined on V. To solve the equation for each K_i, we expand them in a finite element basis compatible with the boundary conditions of the problem, $\{v_l(\boldsymbol{x})\}_{l=1}^n$ (where n is the dimension of the basis, typically $n = n_v = 100$):

$$K(\boldsymbol{x}) = \sum_{l=1}^{n} \alpha_l v_l(\boldsymbol{x})$$

where we simplify the notations, $K(\boldsymbol{x}) = K_i(\boldsymbol{x})$, $i = 1, 2$. Usually this basis is composed of Lagrange polynomial functions. Inserting the expansion of $K(\boldsymbol{x})$ into equation (19), we obtain a linear system of n different equations by taking $v(\boldsymbol{x}) = v_l(\boldsymbol{x})$ for $l = 1, 2, \ldots n$:

$$\sum_{l=1}^{n} G_{jl}\alpha_l = M_j$$

where

$$G_{jl} = \int_V \rho_0(\boldsymbol{x})\nabla v_j(\boldsymbol{x}) \cdot \nabla v_l(\boldsymbol{x}) d\boldsymbol{x},$$

and

$$M_j = \int_V f(\boldsymbol{x}) v_j(\boldsymbol{x}) d\boldsymbol{x},$$

[1] www.fftw.org

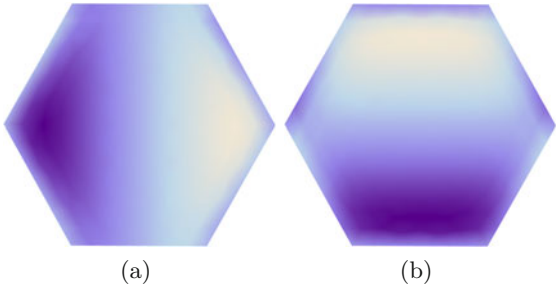

(a) (b)

Fig. 2. (Color online) Density plot of (a) $K_x(x, y)$ and (b) $K_y(x, y)$, calculated directly from a cell of the ground state Figure 1. The parameters are $a = 16$, $\Lambda = 82.36$.

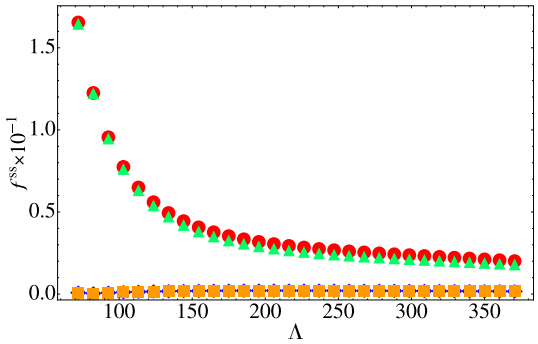

Fig. 3. (Color online) Plot of the different components of the superfluid matrix computed from formula (15) after calculation of the K_x and K_y, as a function of the control parameter Λ. The different plots represent: f^{ss}_{xx}(●), f^{ss}_{xy}(◆), f^{ss}_{yx}(■), f^{ss}_{yy}(▲).

with $f(\boldsymbol{x}) = \partial_i \rho_0(\boldsymbol{x})$. The $K_i(\boldsymbol{x})$ are finally computed by solving this linear system for the n vector $(\alpha_1, \alpha_2, ..., \alpha_n)$. Applying this technique, we plot $K_x(x, y)$ and $K_y(x, y)$ in Figure 2 inside the unit cell of the ground state displayed in Figure 1. Both K_x and K_y have a nodal line that follows directly from (16). Indeed equations (16) may be seen as two Poisson-like equations with "electric charge distributions" $\partial_x \rho_0(x, y)$ and $\partial_y \rho_0(x, y)$ respectively for $K_x(x, y)$ and $K_y(x, y)$. Since $\rho_0(x, y)$ is a symmetric function, its gradient $\partial_x \rho_0(x, y)$ (resp. $\partial_y \rho_0(x, y)$) has a vertical nodal line (resp. horizontal) at the center of the cell. The function K_x (K_y) exhibits thus the following anti-symmetry with this axis $K_x(-x, y) = -K_x(x, y)$ ($K_y(x, -y) = -K_y(x, y)$) where the origin is at the center of the cell. Finally, because of the periodic boundary conditions there is also a nodal curve that matches with the contour of the cell.

Because of the accurate determination of the ground state solution $\rho_0(x, y)$, we are able to compute from the K_i the values of f^{ss} via the formula (15), up to Λ of the order of 400. Every four entries of the 2×2 matrix are plotted in Figure 3. The results exhibit clearly the $x - y$ symmetry whereas the off-diagonal terms (f^{ss}_{xy} and f^{ss}_{yx}) are an order below the diagonal ones (f^{ss}_{xx} and f^{ss}_{yy}). In conclusion, f^{ss} can be correctly approximated by a diagonal matrix:

$$f^{ss} \sim f^{ss}_{xx}\mathcal{I}$$

where $\mathcal{I}$ is the identity matrix in 2-dimensions.

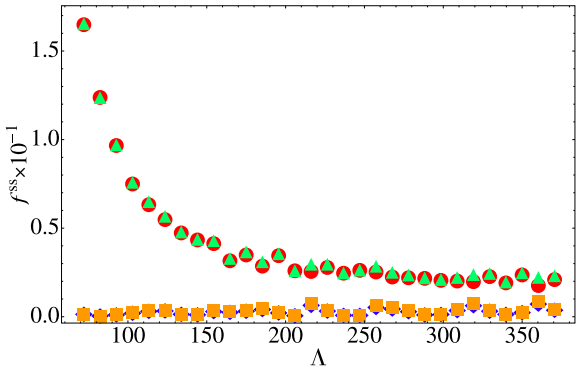

Fig. 4. (Color online) Plot of the different components of the superfluid matrix: f^{ss}_{xx}(•), f^{ss}_{xy}(♦), f^{ss}_{yx}(■), f^{ss}_{yy}(▲) as a function of Λ.

4.3 Direct numerical computation of the superfluid density

An alternative and complementary way to compute the superfluid density is by direct numerical simulation of the GP equation (9). A natural way to mimic the superfluid experiment [41] consists of imposing a given boost $\boldsymbol{v}$ to the system. The resulting current is then related to the superfluid fraction f^{ss}_{ik}. The stationary state is obtained by minimizing the free energy:

$$\mathcal{F} = \mathcal{E} + \boldsymbol{v}\cdot\boldsymbol{\mathcal{P}} + \mu\,(\mathcal{N}-1),$$

where $\boldsymbol{\mathcal{P}}$ is the dimensionless linear momentum deduced from (4). We have to keep in mind that the minimization of the free energy is in the moving reference frame, so that we need to substract from the total momentum the bulk momentum density $m\boldsymbol{v}\int\rho_0(\boldsymbol{x})\,d\boldsymbol{x}$. The superfluid fraction follows then from the momentum computed in the stationary state:

$$f^{ss}_{ik} = \delta_{ik} - \lim_{|\boldsymbol{v}|\to 0}\frac{1}{\int\rho_0(\boldsymbol{x})\,d\boldsymbol{x}}\frac{\partial\mathcal{P}_i}{\partial v_k}. \qquad (20)$$

Figure 4 shows the four elements f^{ss}_{xx}, f^{ss}_{xy}, f^{ss}_{yx}, f^{ss}_{yy} of the superfluid fraction matrix as a function of the parameter Λ by this direct numerical simulation. As a consequence of the imposed boost $\boldsymbol{v}\neq 0$ in the numerics, the resulting curves are noisier than those obtained previously in Figure 3. The same kind of numerical limitations were already observed in 1-dimension [31]. Again, we observe that the results present the $x-y$ symmetry and that the matrix is dominated by the diagonal terms so that f^{ss} can be approximated by a multiple of the identity matrix $\mathcal{I}$. This isotropic property of the matrix can be exhibited by measuring the anisotropy parameter $(f^{ss}_1 - f^{ss}_2)/(f^{ss}_1 + f^{ss}_2)$, where f^{ss}_1 and f^{ss}_2 are the eigenvalues of the superfluid fraction matrix. We have found that in all our results, this anisotropy is always smaller than 10%, even in the large Λ limit where the error bars and fluctuations are higher. We observe also that the anisotropy is lower for larger systems.

Comparing the eigenvalues of the superfluid fraction matrix computed by formula (15) with those obtained by direct numerical simulation (20), we show a good agreement between the two methods in Figure 5. The agreement is particularly good up to $\Lambda\sim 150$ while the fluctuations in the direct measurements affect the comparison above $\Lambda\sim 150$, although the trend is continued. Despite this lack of precision in the direct method, we have demonstrated that both methods are equivalent, as already shown in 1-dimension [31]. In 1-dimension, we have exhibited an exponential decrease of the superfluid fraction with the square-root of the control parameter $\log f^{ss}\propto -\Lambda^{1/2}$ [31], as predicted by the Leggett estimates of superfluid density [27,39]. This estimate has been shown to be valid to higher spatial dimensions [39] but it corresponds then to a lower bound of the superfluid fraction only. In our numerics, we observe that this exponential behavior is still valid in 2D at least for $\Lambda < 150$ as shown in Figure 5b. For higher values of Λ, it is harder to draw strong conclusions from our results and a best fit would rather give a power law decrease $f^{ss}\propto\Lambda^{-0.6}$ than the exponential law. At this stage we have no clear and definite explanation for this apparent change of behavior although a few propositions can be discussed: it is likely that the fluctuations in our numerics do not allow us to discriminate strongly between the two behaviors; on the other hand, the

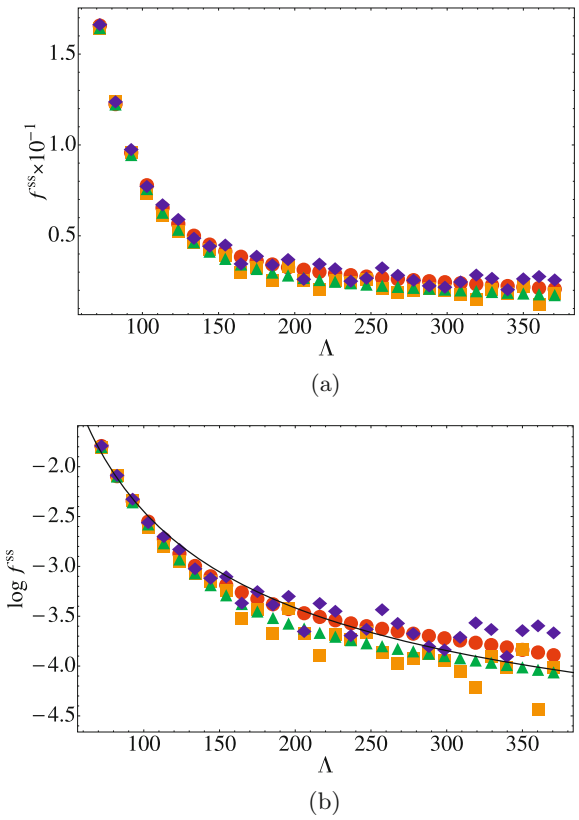

Fig. 5. (Color online) Comparison between eigenvalues of the matrix f^{ss} calculated by the homogenization formula (15) (•, ▲) and by direct computation of the matrix (20) (♦, ■). (a) Plots the eigenvalues of f^{ss} as function of Λ and (b) plots the logarithm (log) of the eigenvalues. The solid line indicates the exponential fit $\log f^{ss}\propto -\Lambda^{1/2}$ as suggested by the theory.

exponential decrease only describes a lower bound based on the density profile of the ground state. It does not account for the multiple paths that can follow the superflow in more than 1-dimension since the superflow could indeed be enhanced by finding its way along the low density regions of the solid.

5 Defects-enhaced superfluid density

The suspected dependence of the supersolid fraction on the specific structure of the crystal lattice is expected to be more pronounced in the presence of defects or vacancies in the model. The dynamics of the vacancies is in fact at the heart of the Andreev-Lifshitz model of a supersolid [1] and it might be important to quantify it in our mean-field approach. In order to tackle the role and the influence of defects for superfluidity, we will now investigate different situations where defects are present. For that purpose, we cannot use the homogenization technique since it applies only for quasi-periodic structures. As explained above, we will rather in this case use the direct numerical simulation imposing a galilean boost to the structure to measure the superfluid fraction. We focus on two distinct configurations that represent the two main types of defect structures. The first one is obtained by starting a GL computation with random initial conditions so that only a few stable defects remains in the domain. The other case consists of a grain boundary crossing the whole domain.

5.1 Random defects

We use a fixed range of interaction $a = 8$ for a value of $\Lambda = 128.68$. We start with the unstable homogenous state to which a random perturbation of small amplitude is added: $\psi = 1 + \text{noise}$ (this initial wave function is normalized to the unit average density). Under the dissipative dynamics (18), we converge to (quasi-)stationary (metastable-)solutions that exhibit defects. These solutions are local minimizers of the Hamiltonian (the global one is free of defects and corresponds to the periodic crystal structure) and are usually metastable. The defects can disappear after very long dynamics (much slower than the time we use to measure the superfluid fraction) by double-annihilation or by adding noise. To measure NCRIF, the solution with defects can thus be considered as a steady state. Among the numerous initial conditions that we have performed, we have selected two representative situations where defects are present, shown in Figure 6: two isolated defects, Figure 6i and a more complex network of defects, modeling roughly a grain boundary (Fig. 6ii).

We thus compute the f^{ss} matrix, via (20), for these two situations. We find that, again, the superfluid matrix is almost diagonal and isotropic (up to 2% of relative variations) as shown in Table 1. Moreover, while the case with only two defects (i) shows only a small increase of the superfluid fraction (about 2%), the more complex configuration of (ii) presents the enhancement of the superfluidity by more than 15%.

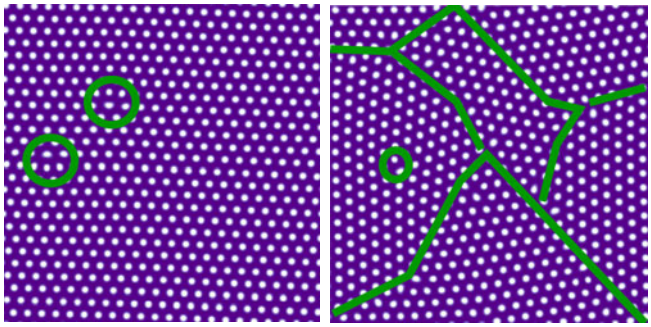

Fig. 6. (Color online) Stationary state corresponding to two random initial conditions (box size is 256×256), (i) represents a state with only two points defects of the crystal pattern. (ii) shows f a complex network (sketched roughly by hand) of defects that forms a randomly oriented boundary grain.

Table 1. The eigenvalues of the matrix f^{ss} for two random initial conditions. We see an increment in the f^{ss} for the cases when a macroscopic network of defects in the crystals are presents. In these simulations the box size is 256×256 units, a range of interaction of $a = 8$ and $\Lambda = 128.68$.

	f_1^{ss}	f_2^{ss}
(i)	0.052	0.052
(ii)	0.059	0.058
Perfect crystal	0.051	0.051

5.2 Grain boundary

It is tempting to investigate a situation where an ordered grain boundary is introduced in the system. To realize such a situation, we consider a modulated structure made by the adjunction of two monocrystals having different orientational order, one with $(1, 0, 0)$ and the second one with crystalline order $(3, 2, 0)$, as shown in Figure 7. To create these crystals, we consider the following different wave functions:

$$\begin{aligned}
\psi_0^{(1)}(\boldsymbol{x}) &= 1 + \epsilon\Big(\cos(k\,y) + \cos\Big(k\,(x\sqrt{3} + y)/2\Big) \\
&\quad + \cos\Big(k\,(x\sqrt{3} - y)/2\Big)\Big) \\
\psi_0^{(2)}(\boldsymbol{x}) &= 1 + \epsilon\Big(\cos(k\,x) + \cos\Big(k\,(x + y\sqrt{3})/2\Big) \\
&\quad + \cos\Big(k\,(x - y\sqrt{3})/2\Big)\Big) \\
\psi_0^{(3)}(\boldsymbol{x}) &= \begin{cases} \psi_0^{(1)}(\boldsymbol{x}) & \forall\, x,\ 0 < y < \frac{L}{2} \\ \psi_0^{(2)}(\boldsymbol{x}) & \forall\, x,\ \frac{L}{2} < y < L \end{cases} \\
\psi_0^{(4)}(\boldsymbol{x}) &= \begin{cases} \psi_0^{(1)}(\boldsymbol{x}) & \forall\, y,\ 0 < x < \frac{L}{2} \\ \psi_0^{(2)}(\boldsymbol{x}) & \forall\, y,\ \frac{L}{2} < x < L, \end{cases}
\end{aligned} \tag{21}$$

where $\psi_0^{(1)}$ and $\psi_0^{(2)}$ represent two initial perfect hexagonal strucutre with a lattice mesh size of $2\pi/k$ units. The relative orientation between the lattices generated by $\psi_0^{(1)}$ and $\psi_0^{(2)}$ is represented by an angle of 30°. We use

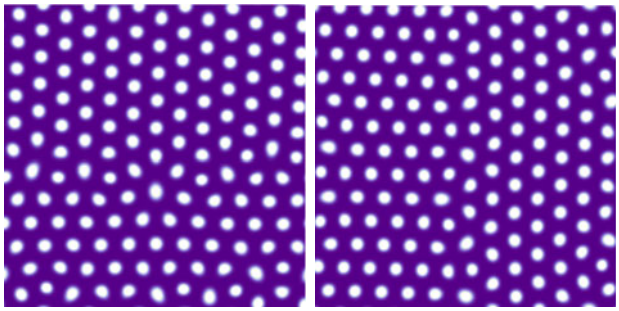

Fig. 7. (Color online) Stationary state corresponding to the initial conditions: (i) $\psi_0^{(3)}$; (ii) $\psi_0^{(4)}$ (box size 128×128). The interaction range is $a = 8$ and $\Lambda = 128.68$.

$k = 0.65$ which is about the highest unstable wave number for $\Lambda = 128.68$ and we take $\epsilon = 0.1$ to initiate the instability that creates the crystal. Finally, each of the wave functions $\psi_0^{(3)}$ and $\psi_0^{(4)}$ contains two grain boundaries located on the x and y axes respectively (one is in the middle of the sample, the other at one of the borders because of the periodic boundary conditions).

We compare now the matrices f^{ss} obtained for the two perfect crystals issued of the initial wave functions $\psi_0^{(1)}$ and $\psi_0^{(2)}$ with those of the composite crystals $\psi_0^{(3)}$ and $\psi_0^{(4)}$. For the perfect crystals we used again the homogenous based techniques while only the boost method (20) could be used for the composite crystals. Since the superfluid fraction matrices are again almost diagonal, we show in Figure 8 the eigenvalues f_1^{ss} and f_2^{ss} only, for the four different states for different values of Λ and for two different system sizes, (i) 128×128 and (ii) 256×256. In all cases, the isotropy is conserved, although the existing grain boundaries are oriented. We also observe that the presence of the grain boundaries always increases the superfluid fraction. However, this effect is higher for the small system (Fig. 8i) than for the large one (Fig. 8ii). One can argue that when the size of the mono-crystal domain increases, the superfluid fraction should converge to the perfect crystal one.

The difference Δf^{ss} between the composite and the perfect crystals appears to depend only slightly on the value of the parameter Λ so that it can represent up to 50% of the superfluid fraction for the small system at high Λ. We propose a simple argument to explain the behavior of the excess superfluid fraction Δf^{ss} on the sample size. Based on the numerical results, we make the assumption that Δf^{ss} is proportional to the fraction of grain boundary:

$$\Delta f^{ss} \sim \frac{\ell d}{L^2} \sim \frac{a}{L}, \tag{22}$$

where ℓ is the length of the grain boundary in the system of typical thickness d. Assuming $\ell \sim L$ while d is of the order of the crystal mesh a, we finally have:

$$\Delta f^{ss} \sim \frac{a}{L}. \tag{23}$$

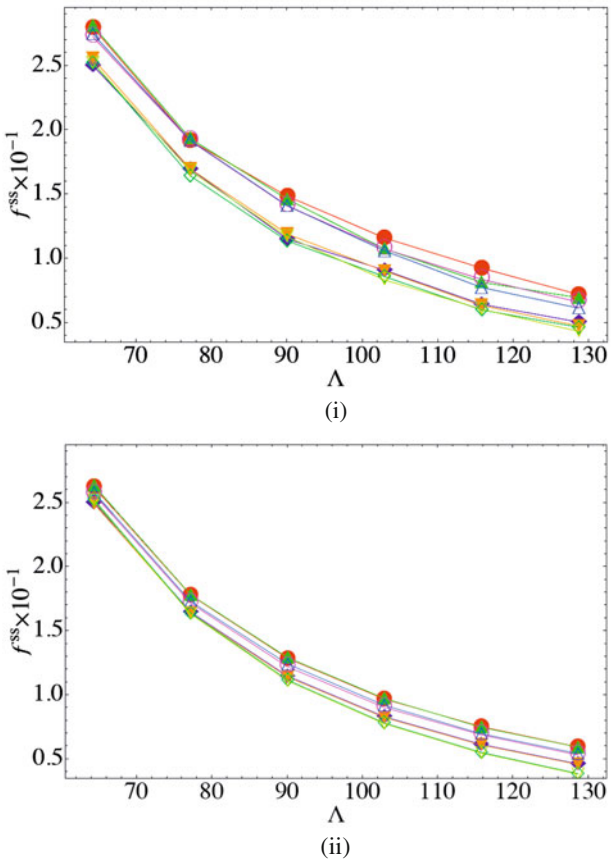

Fig. 8. (Color online) Plot of the eigenvalues of the matrix f^{ss} for the four initial condition considered and for a box size (i) 128×128 and (ii) 256×256. Initial states ψ_0^1(♦)(◇) and ψ_0^2(▼)(▽) correspond to two perfect crystal with different orientations. The states ψ_0^3(●)(○) and ψ_0^4(▲)(△) correspond to two crystalline states with a grain boundaries parallel to the axe x and y respectively.

Remarkably, this argument would be also valid in 3-dimensions.

We end this article by considering the effect of thermal fluctuations. The case of 2-dimensions is known to be critical with respect to long range order with continuous symmetry, which is the case of the present model because it possesses an $U(1)$ symmetry [42,43]. The long-wave acoustic modes are easily excited by thermal fluctuations in the low temperature regime and that would destroy the phase coherence. Indeed, the phase fluctuations diverge logarithmically with the distance while the spatial correlations decay eventually algebraically. This is however not a fundamental objection here since we are considering finite size systems and $T = 0$ dynamics. Moreover, 2-dimensions Bose-Einstein condensates with a superfluid state have been observed experimentally. For such dilute gas systems the same argument on the breakdown of phase coherence at large should apply, but this shows that such effects can in fact be neglected practically there. Finally, in 3-dimensions, the phase fluctuations grow quadratically in temperature and are lower if compression (density) increases [25].

6 Conclusion

In this work, we have presented a detailed study on the superfluid fraction in a model of a supersolid. We have developed two different methods to compute this superfluid fraction applied to the Gross-Pitaevskiĭ mean-field theory. As shown in references [26,28] the superfluid fraction depends explicitly on the ground state wave function of the system. Since no simple analytical relation can be drawn out of the ground state, we have performed a numerical method based on auxiliary functions. The advantage of this method is that it is local, and can be used easily if the ground state is periodic in space. On the other hand, the direct numerical computation of the superfluid fraction using a galilean boost provides an alternative global method. We have demonstrated here that the two methods agree in 2D and that the semi-analytical method is more accurate than the direct numerical simulation method. Using the second method, we have investigated the role of defects in the superfluid fraction. For isolated random defects the superfluid fraction is only little increased but it is clearly enhanced when a grain boundary crosses the sample. Our results are in agreement with a slightly superfluid increase inversely proportional to the length of the mono-crystal present in the sample.

It is our pleasure to thank Olivier Devauchelle and Peter Mason for their help. This work has been supported by the grant ANR-08-SYSC-004 of the Agence National de la Recherche, France (ANR COSTUME). N.S. acknowledges the financial support of CONICYT (Chile) and Foundation Pierre-Gilles de Gennes and S.R. also thanks the FONDECYT grant 1100289 (Chile).

References

1. A.F. Andreev, I.M. Lifshitz, Sov. Phys. JETP. **29**, 1107 (1969)
2. L. Reatto, Phys. Rev. **183**, 334 (1969)
3. G.V. Chester, Phys. Rev. A **2**, 256 (1970)
4. A.J. Leggett, Phys. Rev. Lett. **25**, 1543 (1970)
5. E. Kim, M.H.W. Chan, Nature (London) **427**, 225 (2004)
6. E. Kim, M.H.W. Chan, Science **305**, 1941 (2004)
7. E. Kim, M.H.W. Chan, Phys. Rev. Lett. **97**, 115302 (2006)
8. A.S. Rittner, J.D. Reppy, Phys. Rev. Lett. **97**, 165301 (2006)
9. A.S. Rittner, J.D. Reppy, Phys. Rev. Lett. **98**, 175302 (2007)
10. Y. Aoki, J.C. Graves, H. Kojima, Phys. Rev. Lett. **99**, 015301 (2007)
11. A. Penzev, Y. Yasuta, M. Kubota, J. Low Temp. Phys. **148**, 677 (2007)
12. M. Kondo, S. Takada, Y. Shibayama, K. Shirahama, J. Low Temp. Phys. **148**, 695 (2007)
13. B. Hunt, E. Pratt, V. Gadagkar, M. Yamashita, A.V. Balatsky, J.C. Davis, Science **324**, 632 (2009)
14. D.M. Ceperley, B. Bernu, Phys. Rev. Lett. **93**, 155303 (2004)
15. N. Prokof'ev, B. Svistunov, Phys. Rev. Lett. **94**, 155302 (2005)
16. M. Boninsegni, A.B. Kuklov, L. Pollet, N.V. Prokofev, B.V. Svistunov, M. Troyer, Phys. Rev. Lett. **97**, 080401 (2006)
17. M. Greiner, O. Mandel, T. Esslinger, T.W. Hänsch, I. Bloch, Nature (London) **415**, 39 (2002)
18. O. Morsch, M. Oberthaler, Rev. Mod. Phys. **78**, 179 (2006)
19. K. Goral, L. Santos, M. Lewenstein, Phys. Rev. Lett. **88**, 170406 (2002)
20. T. Lahaye, C. Menotti, L. Santos, M. Lewenstein, T. Pfau, Rep. Prog. Phys. **72**, 126401 (2009)
21. F. Cinti, P. Jain, M. Boninsegni, A. Micheli, P. Zoller, G. Pupillo, Phys. Rev. Lett. **105**, 135301 (2010)
22. N. Henkel, R. Nath, T. Pohl, Phys. Rev. Lett. **104**, 195302 (2010)
23. E.P. Gross, J. Math. Phys. **4**, 195 (1963)
24. L.P. Pitaevskiĭ, Sov. Phys. JETP **13**, 451 (1961)
25. Y. Pomeau, S. Rica, Phys. Rev. Lett. **72**, 2426 (1994)
26. C. Josserand, Y. Pomeau, S. Rica, Phys. Rev. Lett. **98**, 195301 (2007)
27. A.J. Leggett, J. Stat. Phys. **93**, 927 (1998)
28. C. Josserand, Y. Pomeau, S. Rica, Eur. Phys. J.S.T. **146**, 47 (2007)
29. P.W. Anderson, Science **324**, 631 (2009)
30. D.T. Son, Phys. Rev. Lett. **94**, 175301 (2005)
31. N. Sepúlveda, C. Josserand, S. Rica, Phys. Rev. B **77**, 054513 (2008)
32. A.J. Leggett, Science **305**, 1921 (2004)
33. P.W. Anderson, W.F. Brinkman, D.A. Huse, Science **310**, 1164 (2005)
34. N. Prokof'ev, Adv. Phys. **56**, 381 (2007)
35. N.N. Bogoliubov, J. Phys. USSR **11**, 23 (1947)
36. D.A. Kirzhnits, Yu.A. Nepomnyashchii, ZETF **59**, 2203 (1970) [Sov. Phys. JETP **32**, 1191 (1971)]
37. Yu.A. Nepomnyashchii, Theor. Math. Phys. **8**, 928 (1971)
38. Yu.A. Nepomnyashchii, A.A. Nepomnyashchii, Theor. Math. Phys. **9**, 1033 (1971)
39. A. Aftalion, X. Blanc, R.L. Jerrard, Phys. Rev. Lett. **99**, 135301 (2007)
40. A. Bensoussan, J.L. Lions, G. Papanicolaou, *Asymptotic Analysis in Periodic Structures* (North-Holland, Amsterdam, 1978)
41. E.L. Andronikashvili, Zh. Eksp. Teor. Fiz. **16**, 780 (1946)
42. N.D. Mermin, H. Wagner, Phys. Rev. Lett. **17**, 1133 (1966)
43. P.C. Hohenberg, Phys. Rev. **158**, 383 (1967)